

# Scaling Machine Learning Interatomic Potentials with Mixtures of Experts

Yuzhi Liu<sup>1</sup>, Duo Zhang<sup>1,2,3</sup>, Anyang Peng<sup>1</sup>, Weinan E<sup>1,3,4</sup>, Linfeng Zhang<sup>1,2\*</sup>, Han Wang<sup>5,6\*</sup>

<sup>1</sup>AI for Science Institute, Beijing 100080, P. R. China.

<sup>2</sup>DP Technology, Beijing 100080, P. R. China.

<sup>3</sup>Academy for Advanced Interdisciplinary Studies, Peking University, Beijing 100871, P. R. China.

<sup>4</sup> School of Mathematical Sciences, Peking University, Beijing 100871, P. R. China .

<sup>5</sup>National Key Laboratory of Computational Physics, Institute of Applied Physics and Computational Mathematics, Fenghao East Road 2, Beijing 100094, P.R. China.

<sup>6</sup>HEDPS, CAPT, College of Engineering, Peking University, Beijing 100871, P.R. China.

\*Corresponding author(s). E-mail(s): [zhanglf@aisi.ac.cn](mailto:zhanglf@aisi.ac.cn); [wang\\_han@iapcm.ac.cn](mailto:wang_han@iapcm.ac.cn);

## Abstract

Machine Learning Interatomic Potentials (MLIPs) enable accurate large-scale atomistic simulations, yet improving their expressive capacity efficiently remains challenging. Here we systematically develop Mixture-of-Experts (MoE) and Mixture-of-Linear-Experts (MoLE) architectures for MLIPs and analyze the effects of routing strategies and expert designs. We show that sparse activation combined with shared experts yields substantial performance gains, and that nonlinear MoE formulations outperform MoLE when shared experts are present, underscoring the importance of nonlinear expert specialization. Furthermore, element-wise routing consistently surpasses configuration-level routing, while global MoE routing often leads to numerical instability. The resulting element-wise MoE model achieves state-of-the-art accuracy across the OMol25, OMat24, and OC20M benchmarks. Analysis of routing patterns reveals chemically interpretable expert specialization aligned with periodic-table trends, indicating that the model effectively captures element-specific chemical characteristics for precise interatomic modeling.

## 1 Introduction

Over the past few years, MLIPs have rapidly advanced as a powerful strategy to bridge the divide between the high accuracy of Quantum Mechanical (QM) methods and the computational efficiency of classical force fields[1–13]. The fundamental principle of MLIPs

lies in approximating the high-dimensional Potential Energy Surface(PES) by learning from extensive datasets generated via first-principles calculations, such as Density Functional Theory(DFT) [13–18]. Once trained, these potentials can be employed in large-scale molecular dynamics(MD) simulations, enabling the study of complex atomistic processes at a fraction of the computational cost of direct QM approaches [4, 8–10]. As a result, MLIPs have found

successful applications across diverse fields, including drug discovery [19–22], materials science [23–27], and catalysis design [28–30], providing a scalable and accurate framework for exploring chemical space and predicting material properties.

To more accurately model interatomic interactions, a variety of pioneering neural network architectures, such as MACE [31], SevenNet [32], DPA [33, 34], eSEN [35], and AlphaNet [36], have been developed. In pursuit of broader applicability, researchers have progressively scaled up model parameters and trained these architectures on increasingly large datasets, often employing multi-task learning strategies [34, 37, 38]. A notable observation emerging from these efforts is the presence of scaling laws: similar to trends observed in Large Language Models (LLMs) [39, 40], the performance of these interatomic potentials improves predictably with increases in both model size and training data volume [37, 41]. This scaling behavior provides a clear and encouraging roadmap for advancing the accuracy and capability of future machine-learned potentials.

Despite the clear benefits of scaling, simply expanding model capacity through deeper or wider dense architectures remains computationally prohibitive in practice. Two primary bottlenecks hinder this approach: first, the all-to-all computational dependency in dense models limits parallel efficiency [42, 43]; Second, as depth and width increase, the optimization landscape grows increasingly complex, resulting in diminishing returns and heightened training instability [39, 40].

To circumvent these limitations, MoE architectures have emerged as a cornerstone of large-scale modeling [44–49]. An MoE layer replaces the standard dense feed-forward network with a collection of independent experts, governed by a learnable routing mechanism that activates only a sparse subset of parameters for any given input. This design effectively decouples the total model capacity from the computational cost per token [44, 46]. Architecturally, MoE is inherently more conducive to parallelism; by distributing experts across different devices, it reduces the communication bottlenecks typical of standard model parallelism. Consequently, for a fixed computational budget, an MoE model can leverage a significantly larger total parameter count to achieve lower validation loss and superior representational power compared to its dense counterparts [45, 47, 48, 50].

Although this scaling paradigm is highly attractive for MLIPs, its direct adoption faces two fundamental challenges. First, standard MoE designs are often incompatible with the equivariant representations employed by MLIP architectures based on equivariant graph neural networks (GNN), such as MACE [31],

SevenNet [32], eSEN [35], and AlphaNet [36]. Second, unlike the discrete token representations in language models, where sparse expert activation is natural, MLIPs model continuous potential energy surfaces. Abrupt expert switching in this setting can introduce numerical instabilities or non-physical discontinuities, potentially violating the law of energy conservation. To address these challenges, the MoLE framework, exemplified by the UMA models, was introduced [37]. MoLE resolves the first issue by employing a linear combination of experts, ensuring compatibility with equivariant representations. However, the absence of nonlinear activation on the expert outputs may limit the expressive capacity of the resulting representations. To address the second issue, MoLE designs expert routing weights to depend only on configuration-level features derived from the chemical species present in the system, with these weights shared across all atoms in a configuration. Consequently, the expert gating remains invariant with respect to atomic positions, preventing abrupt expert switching and ensuring that the predicted PES remains smooth and differentiable. Nevertheless, this global gating assumption precludes the use of distinct expert knowledge for different atomic species within the same configuration, thereby limiting the model’s capacity to model potential energy contributions through element-wise expert routing.

In this work, we propose an MoE-integrated DPA3 MLIP architecture. DPA3 is a graph neural network built on a line-graph series and has demonstrated state-of-the-art accuracy across diverse benchmarks [41], making it a robust baseline for evaluating MoE-based extensions. Crucially, DPA3 employs exclusively invariant node and edge features, which permits valid nonlinear operations on expert outputs and thus enables the seamless incorporation of standard MoE mechanisms within its framework. Since invariant GNNs can be viewed as a special case of equivariant GNNs, the MoLE architecture can also be implemented within DPA3, providing a unified and controlled setting for direct comparisons between MoE and MoLE designs in terms of their effectiveness for scaling MLIP performance. Building on this foundation, we introduce element-wise expert gating, yielding an element-dependent MoE that models potential-energy contributions through species-specific expert routing. In addition, we incorporate a shared-expert mechanism [51], ensuring that a subset of experts is always activated to capture knowledge common across all element types.

The effectiveness and robustness of the proposed MoE design are rigorously validated on the OMol25, OMat24, and OC20M benchmarks, where it achieves substantial improvements over the baseline. Notably,

Principal Component Analysis (PCA) of the expert latent representations reveals that the learned expert distributions spontaneously recover trends consistent with the periodic table, suggesting that the model implicitly encodes fundamental chemical identities to achieve enhanced predictive accuracy.

## 2 Methodology

In this work, we use the DPA3 model architecture to illustrate the incorporation of a MoE design into a MLIP. The same approach can be readily extended to other graph neural networks that employ invariant features, without substantial modification. The model takes as input the atomic coordinates and chemical species, and outputs the total potential energy  $E$  of the system. DPA3 assumes an atom-wise energy decomposition,

$$E = \sum_i E_i, \quad E_i = E_i(v_i^{1,L}), \quad (1)$$

where  $E_i$  denotes the energy contribution of atom  $i$ , which is derived from the final-layer vertex feature  $v_i^{1,L}$ . This feature represents the state of atom  $i$  within the primary graph of the line-graph series after  $L$  update layers. The majority of DPA3 model parameters reside in the dense layers used to construct messages during message passing along graph edges, which connect atom pairs whose interatomic distance falls within a predefined cutoff radius. A detailed description of the DPA3 architecture is provided in Ref. [41].

For each input feature  $x_i$  associated with atom  $i$ , a dense layer computes

$$y_i = \sigma(Wx_i + b), \quad (2)$$

where  $W$  and  $b$  denote the weight matrix and bias vector, respectively,  $\sigma$  is a nonlinear activation function, and  $y_i$  is the resulting output (see also Fig. 1(a)). The representational capacity of the model can be increased by enlarging these dense layers, i.e., by increasing the dimensionality of the weight and bias parameters.

Instead of a single dense transformation, the MoE introduces multiple parallel expert subnetworks, each composed of a relatively smaller dense layer. The contribution of each expert to the output is modulated by gating weights, which are produced by a router that selects appropriate weights for atom  $i$  based on its chemical identity, encoded by the atomic number  $Z_i$ . The experts can be sparsely activated, such that only a subset of experts receives nonzero gating weights for a given atom. In addition, a subset of experts may always be activated with fixed weights independent of chemical species; these are referred to as shared experts, as they capture knowledge common

to all atoms regardless of chemical type. A schematic illustration of the MoE architecture is provided in Fig. 1(b).

Assume that the MoE contains a total of  $N$  experts, consisting of  $I$  routed experts and  $N - I$  shared experts. The MoE transformation is defined as

$$y_i = \sum_{j=1}^I \alpha_{ij} \sigma(W_j x_i + b_j) + \sum_{j=I+1}^N \sigma(W_j x_i + b_j), \quad (3)$$

$$\alpha_{ij} = \begin{cases} s_{ij}, & \text{if } s_{ij} \in \text{TopK}(\{s_{im}\}, K'), \\ 0, & \text{otherwise,} \end{cases} \quad (4)$$

$$s_{ij} = \text{softmax}(W_e u_i), \quad (5)$$

where  $\sigma(\cdot)$  denotes a nonlinear activation function,  $W_j$  and  $b_j$  are the trainable expert-specific weights and bias, and  $\alpha_{ij}$  is the gating weight applied to the  $j$ -th routed expert for atom  $i$ . The operator  $\text{TopK}(\{s_{im}\}, K')$  selects the largest  $K' \leq I$  elements from the set of gating scores  $\{s_{im} \mid 1 \leq m \leq I\}$ , thereby enforcing sparse expert activation. Including the  $(N - I)$  shared experts that are always active, the total number of activated experts is denoted by  $K$ , satisfying

$$K = K' + (N - I). \quad (6)$$

The gating scores  $s_{ij}$  are computed according to equation 5, where  $W_e \in \mathbb{R}^{I \times M}$  is a trainable routing matrix and  $u_i \in \mathbb{R}^M$  is a latent representation of dimension  $M$ , encoding the chemical identity of atom  $i$ .

The hidden representation  $u_i$  is defined as

$$u_i = \text{MLP}(\text{one\_hot}(Z_i)), \quad (7)$$

where the atomic number  $Z_i$  is first mapped to a one-hot vector and subsequently projected into a continuous embedding space via a multilayer perceptron (MLP). This element-wise routing mechanism enables atom-type-dependent expert selection while preserving smoothness and differentiability, which are essential for stable and physically consistent interatomic potential modeling.

In contrast, the UMA model [37] adopts an atom-averaged routing representation that incorporates dataset identifiers along with charge and spin information. In our implementation, we utilize this atom-averaged routing scheme to ensure a fair and consistent comparison with element-wise routing. Specifically, we define a global routing vector through mean pooling:

$$\bar{u} = \frac{1}{N_{\text{atom}}} \sum_i u_i, \quad (8)$$

where the unified representation  $\bar{u}$  is applied across all atoms in the system to determine gating scores. Under this formulation, atomic representations are averaged

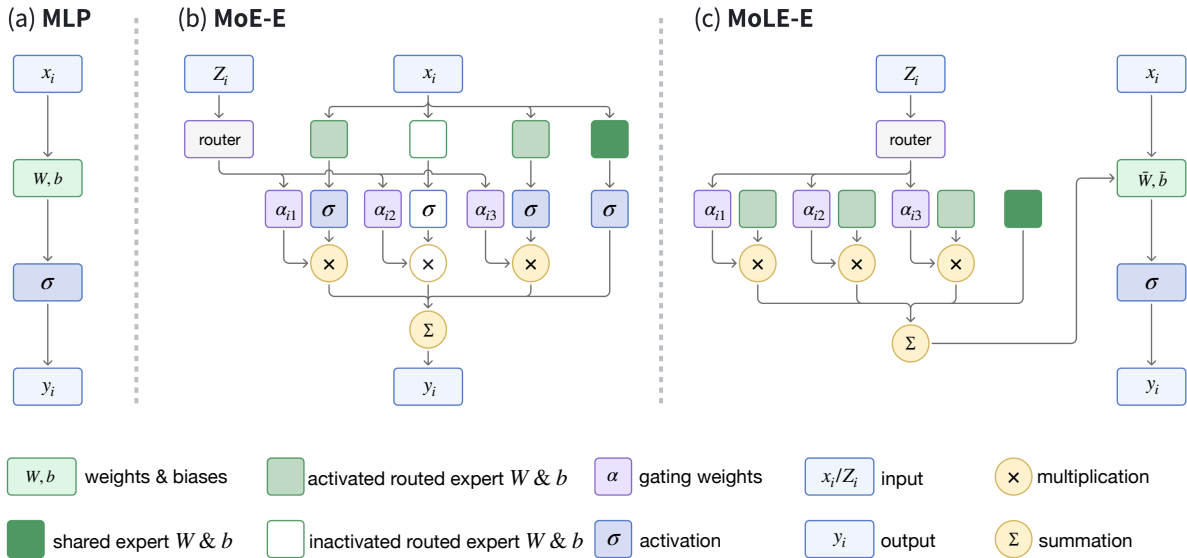


**Fig. 1:** Schematic illustration of the model architectures. (a) The standard MLP framework. (b) The MoE-E framework, featuring a router that dynamically selects 3 active experts from the pool, complemented by 1 fixed shared expert to capture universal features. (c) The MoLE-E framework, where 4 expert weights are linearly combined via the router to modulate the main network weights, including 1 shared expert component.

across the entire configuration, and all atoms share an identical set of gating scores and weights. To distinguish these two routing strategies, we refer to the atom-wise and global (configuration-wise) representations as MoE-E and MoE-G, respectively.

In the MoE formulation, input features are first processed by expert subnetworks and then linearly combined using gating weights. In contrast, in the MoLE formulation the features are first linearly transformed by expert-specific weights, after which the expert contributions are aggregated via gating weights, and a nonlinear activation function is applied at the end, as illustrated in Fig. 1(c). This yields

$$y_i = \sigma \left( \sum_{j=1}^I \alpha_{ij} (W_j x_i + b_j) + \sum_{j=I+1}^N (W_j x_i + b_j) \right), \quad (9)$$

$$\alpha_{ij} = \text{softmax} \left( W_e u_i \right) \quad (10)$$

where  $\sigma(\cdot)$  denotes the activation function. Equation equation 9 is mathematically equivalent to a single dense layer with effective parameters,

$$y_i = \sigma(\bar{W} x_i + \bar{b}), \quad (11)$$

$$\bar{W} = \sum_{j=1}^I \alpha_{ij} W_j + \sum_{j=I+1}^N W_j, \quad (12)$$

$$\bar{b} = \sum_{j=1}^I \alpha_{ij} b_j + \sum_{j=I+1}^N b_j. \quad (13)$$

Thus, MoLE can be interpreted as a data-dependent linear transformation whose weights and biases are modulated by the gating mechanism prior to the nonlinearity.

Analogous to MoE, MoLE admits two variants depending on how chemical identity information is encoded in the router. We denote these as MoLE-E and MoLE-G, corresponding to element-wise and global (configuration-wise) routing representations, respectively.

### 3 results

In this section, we benchmark the proposed MoE-based architectures. To ensure a controlled and consistent comparison, we adopt a standard 6-layer DPA3 model as our baseline, with all hyperparameters detailed in the Supplementary Table 1. Performance is

primarily illustrated using normalized Mean Absolute Error (MAE), while absolute MAE values are provided in the Supplementary Note 2 for comprehensive reference. We evaluate 6-layer variants of MoE and MoLE with both element-wise and global routing, and systematically compare their performance against the baseline to quantify the relative gains enabled by different expert designs. The detailed hyperparameters for the different models are outlined in Supplementary Note 1.

### 3.1 Sparse activation and shared experts

Two important design choices in MoE are **sparse expert activation** and the use of **shared experts**. Figure 2(a) systematically investigates the impact of these design choices using the OMol25 dataset as a benchmark [52]. Covering 83 chemical elements, OMol25 displays remarkable chemical diversity, including complex intermolecular interactions, explicit solvation, variable charge and spin states, as well as reactive configurations. In this experiment, the total number of experts is fixed at  $N = 64$ , while the number of activated experts  $K$  varies from 2 to 8. For each value of  $K$ , multiple configurations with different numbers of shared experts are evaluated.

Overall, model performance improves with increasing  $K$ . In the absence of shared experts, the normalized energy (force) MAEs for  $K = 2, 4, 6$ , and 8 are 1.082 (0.965), 0.965 (0.919), 0.923 (0.902), and 0.926 (0.900), respectively. This trend is primarily driven by the effective linear expansion of model capacity, since a configuration with  $K$  activated experts corresponds to an approximately  $K$ -fold increase in the number of active parameters. However, several non-trivial behaviors are observed. Notably, the  $K = 2$  model without shared experts, despite having roughly twice the parameter count of the baseline, exhibits a degraded energy MAE. In addition, performance saturates between  $K = 6$  and  $K = 8$ , indicating diminishing returns where the additional computational budget no longer translates into measurable accuracy gains. These results suggest that naive scaling of the number of activated experts alone is insufficient.

Across nearly all choices of activated experts  $K$ , introducing shared experts consistently improves model performance. This effect is particularly pronounced for  $K = 8$ , where increasing the number of shared experts from zero to six reduces the normalized MAEs for energy and force by 0.269 and 0.200, respectively. Notably, performance is optimized when the number of shared experts approaches approximately half of the activated experts, as observed for the  $K = 4, 6$ , and 8 configurations. Beyond

this regime, further increasing the fraction of shared experts yields diminishing returns or even slight performance degradation, for example, the force MAE increases when the number of shared experts rises from 2 to 3 in the  $K = 4$  configuration. Overall, these results indicate that allocating roughly half of the activated experts as shared experts provides an effective trade-off between capturing global chemical knowledge common across elements and preserving sufficient capacity for element-specific specialization.

When adopting a configuration in which half of the activated experts are shared, the normalized energy (force) MAEs for  $K = 2, 4, 6$ , and 8 are reduced to 0.939 (0.913), 0.771 (0.779), 0.740 (0.747), and 0.673 (0.715), respectively. In stark contrast to the no-shared-expert setting, the accuracy improvement in this regime does not plateau at  $K = 8$ , but instead continues to scale favorably with increasing model capacity. These results highlight that shared experts are indispensable for effectively exploiting larger expert pools and for achieving stable, monotonic performance scaling. Importantly, for a fixed number of activated experts  $K$ , increasing the number of shared experts does not alter the total parameter count or computational cost. Consequently, the observed accuracy gains from shared experts are achieved at essentially no additional computational overhead.

### 3.2 MoE-E vs MoLE-E

Figure 2(b) presents a comparison between the MoE-E and MoLE-E architectures, both of which maintain an identical parameter count. The fundamental distinction between these two designs lies in the sequencing of the nonlinear transformation relative to expert aggregation: MoE-E applies the activation function locally within each expert before mixing their outputs, whereas MoLE-E performs a linear aggregation of expert contributions followed by a global activation function. Furthermore, while MoE-E utilizes a sparse activation of  $K$  experts, MoLE-E employs a dense approach where all experts are activated. For a controlled comparison, all MoE-E configurations are evaluated with the same number of activated experts ( $K = 4$ ). The normalized energy and force accuracies of the MoE-E and MoLE-E architectures are reported as functions of the total number of experts  $N$ .

Despite the architectural difference between the sparsely activated MoE-E and the fully activated MoLE-E, both models show comparable performance without shared experts. Across various expert scales, the discrepancies in normalized energy and force MAE are negligible, staying within 0.02 and 0.03 respectively. In both architectures, substantial performance gains are observed when increasing the number of

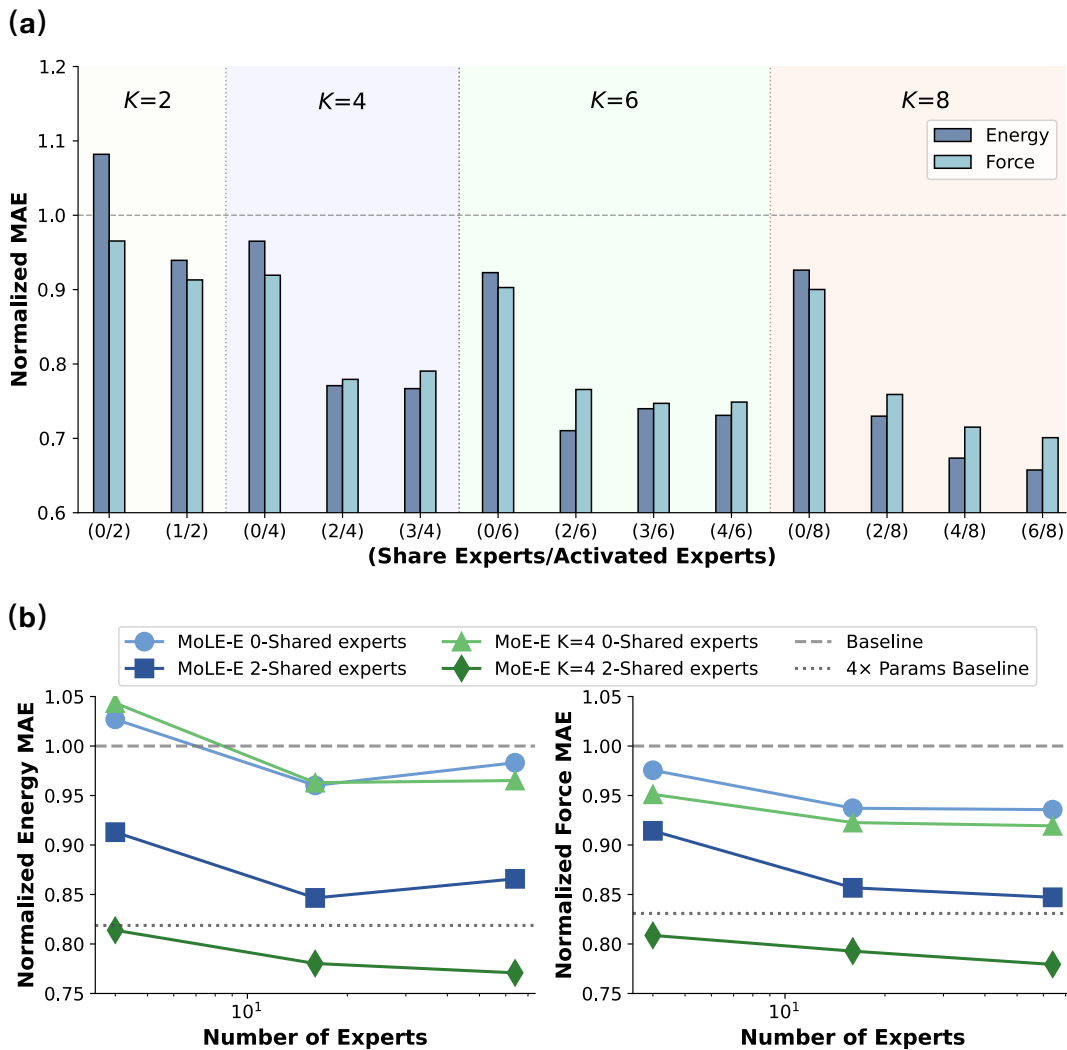


**Fig. 2:** Performance benchmarks on the OMol25 dataset. (a) Impact of shared expert allocation. Normalized energy and force MAE for MoE-E are shown as a function of the shared expert ratio, using a total pool of 64 experts. The x-axis denotes the proportion of shared experts (e.g., (2/6) indicates 2 shared experts among 6 total activated experts). Background shading demarcates different  $K$  activation settings for MoE-E. The horizontal dashed line provides a performance baseline corresponding to a standard 6-layer DPA3 model. See Supplementary Table 2 for detailed values. (b) Scaling with total expert count: Comparative analysis of normalized energy (left) and force (right) MAE as a function of the total number of experts. Two baselines are provided: the standard 6-layer DPA3 model and a “4× Params” variant achieved by doubling the hidden dimension of the 6-layer DPA3 model. See Supplementary Table 3 for detailed values.

experts from  $N = 4$  to  $N = 16$ ; however, the improvement saturates beyond  $N = 16$ , with no significant additional accuracy gains when further increasing the expert count to  $N = 64$ .

The integration of shared experts yields markedly different gains for the two architectures. When two shared experts are introduced, the MoLE-E variant exhibits a reduction in normalized energy MAE of approximately 0.11, accompanied by a decrease in

normalized force MAE ranging from 0.06 to 0.09. Although the force accuracy shows a slight improvement when increasing the total number of experts from  $N = 16$  to  $N = 64$ , the corresponding energy accuracy displays a reversed trend increasing from 0.846 to 0.865, partially offsetting the overall performance gain. In contrast, MoE-E demonstrates a substantially stronger response to the introduction of shared experts. For the same transition from zero to two shared experts, MoE-E achieves a larger reduction in normalized energy MAE, ranging from 0.18 to 0.23, and a decrease in normalized force MAE of approximately 0.13 to 0.14. Moreover, the accuracy of MoE-E continues to improve as the number of experts increases from  $N = 16$  to  $N = 64$ , indicating that the MoE-E architecture can effectively leverage a larger expert pool to achieve further performance gains.

### 3.3 Parameter Efficiency of MoE-E

Since the MoE-E model with four activated experts ( $K = 4$ ) utilizes four times the activated parameters of the baseline, we established a widened dense baseline for a fair comparison. This "4× Params Baseline" was constructed by doubling the dimensionality of all hidden features to match the parameter scale. This 4× Params baseline, yields improvements of 0.181 and 0.169 in normalized energy and force accuracy, respectively, relative to the standard model (Fig. 2(b)). As the total number of experts increases, the MoE-E model with two shared experts consistently outperforms the widened baseline. In particular, with  $N = 64$  experts, MoE-E achieves additional gains of 0.052 and 0.048 in energy and force precision, respectively. These results demonstrate that the sparse-activation strategy in MoE-E provides greater expressive capacity than conventional width-based scaling, enabling higher predictive accuracy than dense architectural scaling under comparable computational budgets.

### 3.4 Element-wise vs Global routing

We perform a comparative analysis of element-wise routing (MoE-E and MoLE-E) and their global counterparts (MoE-G and MoLE-G) on the OMol25 dataset [52]. This breadth provides a stringent benchmark for evaluating the stability and accuracy of different expert-routing strategies across a highly heterogeneous chemical space.

Table 1 summarizes the comparative performance of global and element-wise routing architectures across all architectural variants. In these experiments, we vary the total number of experts  $N$  while fixing the number of activated experts to  $K = 4$ , among which two are shared experts. As shown in Table 1, the

MoE-G architecture suffers from catastrophic training failure: its energy and force MAEs exhibit severe numerical instability and fail to converge. As a result, its accuracy is not reported. For the remaining variants (MoE-E, MoLE-E, and MoLE-G), the energy and force MAEs are reported after normalization by the corresponding MAEs of the baseline standard DPA3 model.

Overall, increasing the number of experts from  $N = 4$  to  $N = 16$  consistently improves both energy and force accuracy across all stable variants. However, further increasing the number of experts from  $N = 16$  to  $N = 64$  yields diminishing returns: performance gains saturate for MoE-E, while accuracy degrades for MoLE-G and for the energy prediction of MoLE-E. Comparing different mixture designs, MoE-E consistently outperforms both MoLE variants across all expert scales. Moreover, MoLE-G systematically underperforms its element-wise counterpart MoLE-E, with MoLE-E achieving approximately 5%–10% lower MAEs in both energy and force predictions across all values of  $N$ . Taken together, these results demonstrate that element-wise routing is structurally superior to global routing and is essential for the stable and effective integration of MoE architectures into MLIPs.

### 3.5 Performance on Multiple Datasets

To comprehensively evaluate the robustness and generalization capability of the proposed MoE-based interatomic potentials, we benchmark the models on several widely recognized datasets, including OMol25 [52], OMat24 [53], and OC20M [30]. These datasets collectively span a broad range of chemical environments and material systems, including organic molecules, extended solid-state materials, and catalytic surface reactions, thereby enabling a representative assessment across multiple domains of computational chemistry and materials science. The inclusion of these diverse benchmarks allows for a rigorous evaluation of model performance under heterogeneous conditions and highlights the transferability, stability, and cross-domain generalization capability of the MoE architecture in realistic applications.

Fig. 3 summarizes model performance across multiple benchmark datasets. For MoE-E, we employ  $K = 6$  activated experts, among which three are shared, with the total number of experts fixed at  $N = 64$ . Our evaluation strategy is designed to explicitly highlight the advantages of MoE-E by comparing it against two distinct configurations. First, to control for the total parameter count, we evaluate it against MoLE-E, which maintains an identical architecture to MoE-E model, specifically configured with 3 shared experts

Model	Routing	Normalized Energy MAE			Normalized Force MAE		
		4 Experts	16 Experts	64 Experts	4 Experts	16 Experts	64 Experts
MoE	Element-wise (E)	0.814	0.780	0.771	0.809	0.793	0.779
	Global (G)	N/A	N/A	N/A	N/A	N/A	N/A
MoLE	Element-wise (E)	0.913	0.847	0.866	0.914	0.857	0.847
	Global (G)	0.981	0.946	0.952	0.965	0.936	0.950

**Table 1:** Normalized Energy and Force MAE values. The results compare the performance of Global (G) vs. Element-wise (E) routing across different expert counts. All MAEs are normalized against a 6-layer DPA3 baseline; thus, values represent relative error ratios where a lower score signifies superior performance relative to the baseline. See Supplementary Table 4 for detailed values.

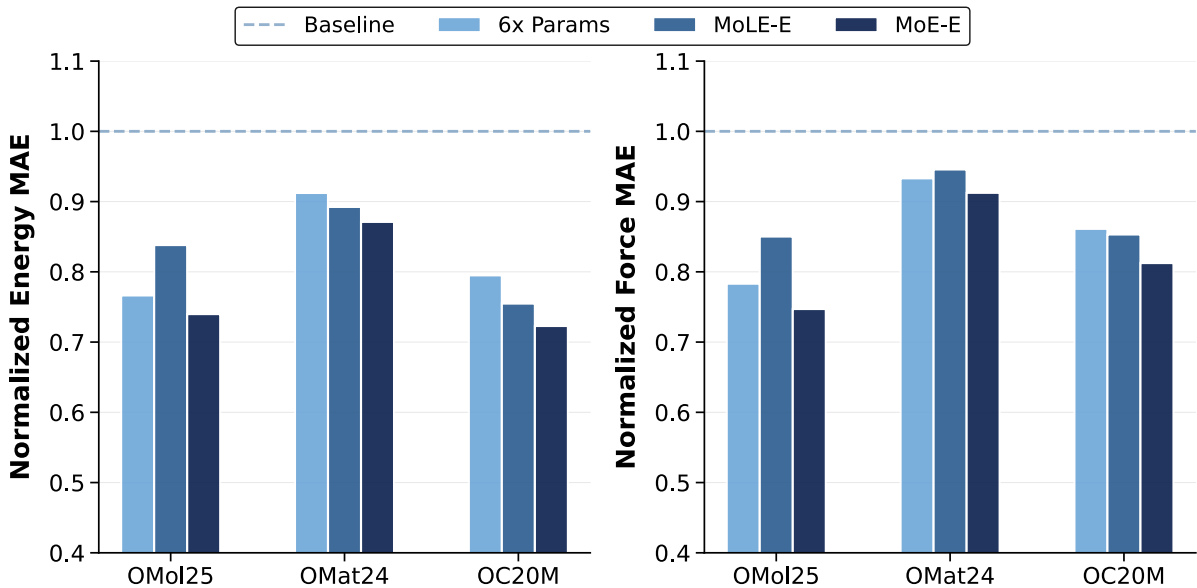


**Fig. 3:** Performance benchmarks for normalized energy (left) and force (right) predictions across three datasets: OMol25, OMat24, and OC20M. The baseline corresponds to the standard DPA3 model, while the “6× Params” is scaled to six times the total parameters of the baseline via wider hidden layers. The MoLE-E model employs 64 experts with 3 shared experts, and the MoE-E model uses 64 experts with 3 shared experts out of  $K = 6$  activated experts. See Supplementary Table 5 for detailed values.

out of a total of 64 experts. Second, we introduce a “6 × Params” model to match the activated parameter count of MoE-E. This model is scaled to six times the total size of the baseline via wider hidden layers, allowing us to compare performance under equivalent computational budgets.

As shown in Fig. 3, all enhanced models—MoE-E, MoLE-E, and the 6× Params model—achieve substantial improvements over the baseline model (indicated

by the horizontal line at 1.0) across all three datasets. Notably, MoE-E consistently outperforms MoLE-E across all evaluated benchmarks, demonstrating its robust generalization capabilities. Specifically, we observed a reduction in normalized Energy MAE by 0.10, 0.02, and 0.03, complemented by a decrease in normalized Force MAE of 0.10, 0.03, and 0.04 on the OMol25, OMat24, and OC20M datasets, respectively. These improvements underscore the superiority

of nonlinear expert aggregation over linear alternatives in capturing complex interatomic potentials. Furthermore, MoE-E even surpasses a dense baseline with  $6\times$  the parameter count, yielding additional error reductions of up to 0.07 in Energy and 0.05 in Force. This highlights the exceptional parameter efficiency inherent to the MoE-E architecture.

Furthermore, we observe that the performance gains yielded by the enhanced models exhibit significant heterogeneity across different datasets. Specifically, the MoE-E model manifests substantial predictive advantages on the OMol25 (molecular) and OC20M (catalytic) benchmarks. However, its efficacy becomes more marginal on the OMat24 (solid-state) dataset, where only a moderate reduction in MAE is recorded. This divergence in performance is primarily ascribed to the inductive biases inherent in the DPA3 backbone.

### 3.6 Experts weighting Distribution Patterns

To gain deeper insights into the interpretability of the MoE-E model, we investigate the distribution patterns of experts weight as defined by the projection  $W_e u_i$ . This analysis aims to elucidate how the routing mechanism allocates learning responsibilities among experts according to elemental characteristics. We conduct this analysis on the OMat24 dataset, which provides an ideal testbed due to its extensive coverage of 86 elements with a relatively uniform distribution across the periodic table.

Principal component analysis (PCA) of the expert-weighting distributions reveals highly efficient dimensionality reduction, with the first two principal components accounting for 93.57% of the total explained variance. Figure 4 presents the projected expert distributions across chemical species, revealing systematic organization in the PCA space [44, 54]. As shown in Fig. 4(a), which illustrates the global distribution of all elements, clear chemical groupings emerge: lanthanides and actinides cluster on the left side of the PCA manifold, while transition metals predominantly occupy the central region.

Figure 4(b) highlights the alkali metals (Group I), alkaline-earth metals (Group II), and noble gases (Group VIII), while Fig. 4(c) focuses on elements from Groups III to VII together with hydrogen. A consistent pattern emerges across chemical groups: elements within the same group arrange themselves diagonally from the top-left to the bottom-right of the PCA space. This spatial ordering correlates strongly with increasing atomic number, with lighter elements located in the top-left region and heavier elements positioned toward the bottom-right.

Along the period direction, as shown in Fig. 4(c), elements with pronounced non-metallic character exhibit a systematic shift from the top-right toward the bottom-left of the PCA space with increasing atomic number. In contrast, strongly metallic elements follow the opposite orientation, extending from the bottom-left (Group I) to the top-right (Group II), as visualized in Fig. 4(b). Elements with intermediate chemical behavior—particularly those in Groups III (Al, Ga, In, Tl) and IV (Si, Ge, Sn, Pb)—display overlapping distributions in the PCA embedding (Fig. 4(c)). Noble gases, although electronically distinct, constitute an exception: their embeddings partially overlap with those of intermediate elements, which may reflect their relatively limited representation in the OMat24 dataset.

As illustrated in Fig. 4(d), transition metals are predominantly concentrated near the center of the PCA space. Within this cluster, elements belonging to the same period exhibit a clear diagonal alignment: as the group number increases, their distributions shift from the top-right toward the bottom-left. This trend is further reflected by the color gradient from dark to light green, capturing the systematic evolution of their electronic characteristics.

These structured distributions demonstrate that the MoE-E router effectively encodes elemental characteristics in a manner consistent with fundamental physicochemical principles. The observed organization—group-wise diagonals, periodic progressions, and the distinct clustering of transition metals and *f*-block elements—indicates that the model internalizes a chemically meaningful representation of the periodic table. This interpretable, element-wise task specialization provides a clear mechanistic explanation for the superior accuracy and generalization of MoE-E. By explicitly leveraging elemental identity to guide expert routing, the model captures sharper distinctions among chemically diverse species while allocating expert capacity more efficiently across compositional space. Such a design bridges learned representations with established chemical intuition, offering a principled and scalable pathway toward more accurate, transferable, and interpretable MLIPs.

## 4 Conclusion

In this work, we present a systematic investigation of MoE architectures for MLIPs and demonstrate that sparsely activated expert scaling provides an effective pathway for improving predictive accuracy beyond conventional dense model enlargement. By integrating

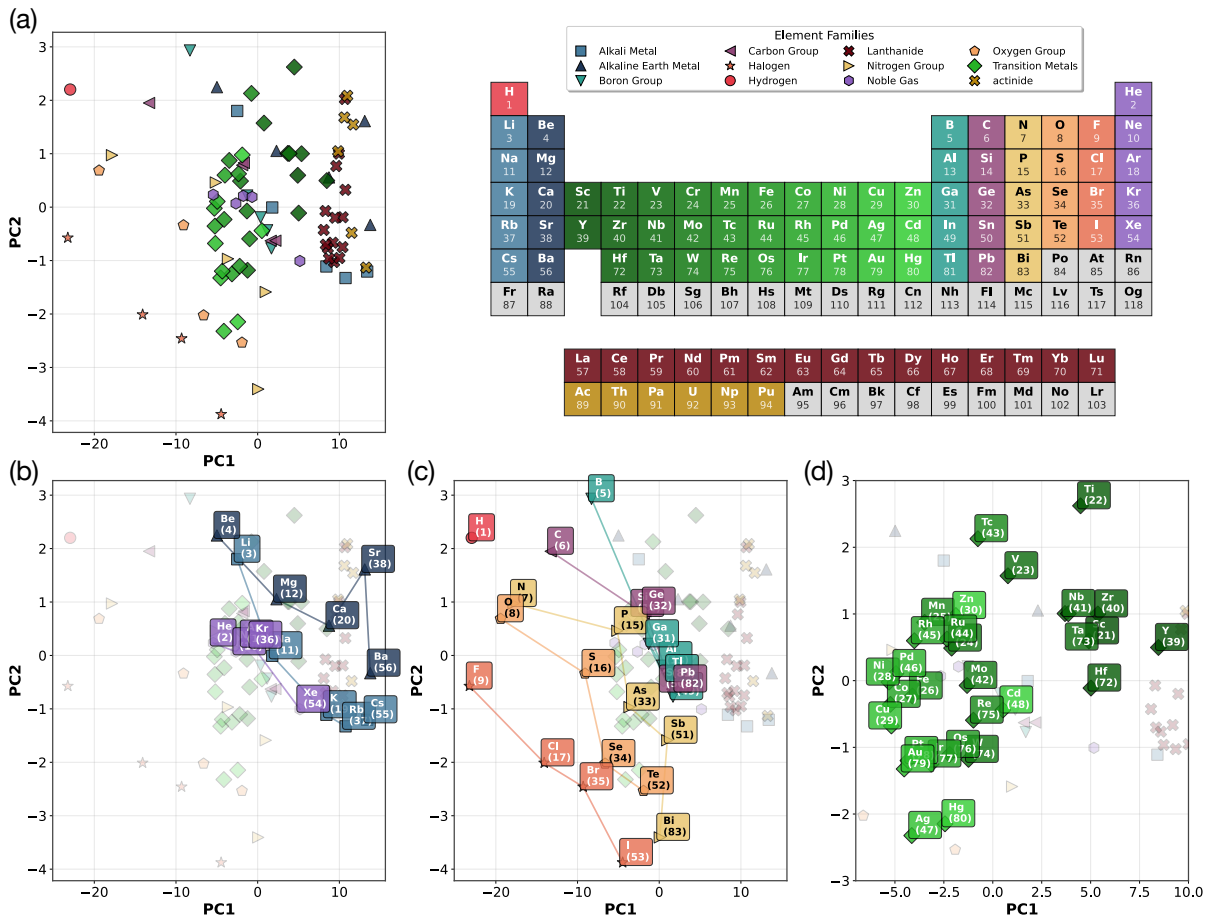


**Fig. 4:** Expert weighting distribution analysis via PCA for various elemental groups. (a) Overview of the general distribution for all elements. (b) Distribution patterns for alkali metals, alkaline earth metals, and noble gases. (c) Regional distribution of p-block groups except noble gas, specifically Boron (Group 13) through Halogen (Group 17) elements. (d) Spatial clustering of transition metal elements.

MoE designs into the DPA3 framework, we demonstrate that sparse activation, shared-expert mechanisms, nonlinear expert specialization, and element-wise expert routing collectively constitute the key ingredients enabling stable and scalable performance gains. Across diverse benchmarks—including OMol25, OMat24, and OC20M—the proposed element-wise MoE architecture consistently achieves substantial improvements in both energy and force prediction accuracy, while also exhibiting interpretable expert specialization patterns that align with periodic chemical trends.

Our analysis provides several conceptual insights into MoE design choices for scaling atomistic foundation models. First, the introduction of sparse activation together with shared experts enables the learning of transferable representations of common interatomic

interactions, allowing efficient utilization of large expert pools. Second, nonlinear expert aggregation delivers greater representational capacity than linear mixture formulations, underscoring the importance of nonlinear specialization for accurately modeling complex potential-energy surfaces. Third, element-wise routing is essential for stable training and effective specialization in chemically heterogeneous systems, consistently outperforming global routing strategies that may introduce optimization instability. Collectively, these findings establish MoE-based conditional computation as a principled alternative to dense parameter scaling for next-generation large atomistic models.

Despite these advances, an important limitation of the present study is that the current implementation does not yet exploit a fully distributed training

and inference framework specifically optimized for sparse expert parallelism. While MoE architectures are intrinsically well-suited for distributed environments and offer substantial theoretical scalability advantages over dense scaling, realizing these benefits in practice requires dedicated expert-parallel system design, communication scheduling, and load-balancing strategies. Future work will therefore focus on developing large-scale distributed MoE training and inference pipelines to unlock the full computational efficiency and scaling potential of expert-based atomistic foundation models.

Overall, this work demonstrates that MoE architectures provide a scalable and physically grounded paradigm for expanding the expressive capacity of MLIP, offering a promising foundation for increasingly accurate and transferable simulations across the chemical and materials sciences.

**Data Availability.** All data supporting the findings of this study are available within the Supplementary Information

**Acknowledgments.** Computational resources utilized in this work were provided by the AI for Science. The work is supported by the National Key R&D Program of China (Grant No. 2022YFA1004300) and the National Natural Science Foundation of China (Grant Nos. 12525113 and 12561160120).

**Competing Interests.** The authors declare no competing interests.

**Author Contribution.** Y.L., D.Z., A.P., H.W. conceived the idea of this work, designed the model structure, and implemented the model. The experiments were mainly designed and performed by Y.L. Other authors performed data collection and model tests on different systems. All authors contributed to the discussions and edited the manuscript.

## References

- [1] Behler, J., Parrinello, M.: Generalized neural-network representation of high-dimensional potential-energy surfaces. *Physical review letters* **98**(14), 146401 (2007)
- [2] Bartók, A.P., Payne, M.C., Kondor, R., Csányi, G.: Gaussian approximation potentials: The accuracy of quantum mechanics, without the electrons. *Physical review letters* **104**(13), 136403 (2010)
- [3] Rupp, M., Tkatchenko, A., Müller, K.-R., Von Lilienfeld, O.A.: Fast and accurate modeling of molecular atomization energies with machine learning. *Physical review letters* **108**(5), 058301 (2012)
- [4] Zhang, L., Han, J., Wang, H., Car, R., E, W.: Deep potential molecular dynamics: a scalable model with the accuracy of quantum mechanics. *Physical review letters* **120**(14), 143001 (2018)
- [5] Schütt, K.T., Sauceda, H.E., Kindermans, P.-J., Tkatchenko, A., Müller, K.-R.: Schnet—a deep learning architecture for molecules and materials. *The Journal of chemical physics* **148**(24) (2018)
- [6] Gasteiger, J., Groß, J., Günnemann, S.: Directional message passing for molecular graphs. *arXiv preprint arXiv:2003.03123* (2020)
- [7] Batzner, S., Musaelian, A., Sun, L., Geiger, M., Mailoa, J.P., Kornbluth, M., Molinari, N., Smidt, T.E., Kozinsky, B.: E (3)-equivariant graph neural networks for data-efficient and accurate interatomic potentials. *Nature communications* **13**(1), 2453 (2022)
- [8] Deringer, V.L., Caro, M.A., Csányi, G.: Machine learning interatomic potentials as emerging tools for materials science. *Advanced Materials* **31**(46), 1902765 (2019)
- [9] Unke, O.T., Chmiela, S., Sauceda, H.E., Gastegger, M., Poltavsky, I., Schütt, K.T., Tkatchenko, A., Müller, K.-R.: Machine learning force fields. *Chemical Reviews* **121**(16), 10142–10186 (2021)
- [10] Mishin, Y.: Machine-learning interatomic potentials for materials science. *Acta Materialia* **214**, 116980 (2021)
- [11] Čížek, J.: On the correlation problem in atomic and molecular systems. calculation of wavefunction components in urself-type expansion using quantum-field theoretical methods. *The Journal of Chemical Physics* **45**(11), 4256–4266 (1966)

- [12] White, S.R.: Density matrix formulation for quantum renormalization groups. *Physical review letters* **69**(19), 2863 (1992)
- [13] Ceperley, D.M., Alder, B.J.: Ground state of the electron gas by a stochastic method. *Physical review letters* **45**(7), 566 (1980)
- [14] Hohenberg, P., Kohn, W.: Inhomogeneous electron gas. *Physical review* **136**(3B), 864 (1964)
- [15] Kohn, W., Sham, L.J.: Self-consistent equations including exchange and correlation effects. *Physical review* **140**(4A), 1133 (1965)
- [16] Andolina, C.M., Saidi, W.A.: Highly transferable atomistic machine-learning potentials from curated and compact datasets across the periodic table. *Digital Discovery* **2**(4), 1070–1077 (2023)
- [17] Perdew, J.P., Burke, K., Ernzerhof, M.: Generalized gradient approximation made simple. *Physical review letters* **77**(18), 3865 (1996)
- [18] Becke, A.D.: Density-functional thermochemistry. iii. the role of exact exchange. *The Journal of chemical physics* **98**(7), 5648–5652 (1993)
- [19] Badaoui, M., Buigues, P.J., Berta, D., Mandana, G.M., Gu, H., Foldes, T., Dickson, C.J., Hornak, V., Kato, M., Molteni, C., *et al.*: Combined free-energy calculation and machine learning methods for understanding ligand unbinding kinetics. *Journal of chemical theory and computation* **18**(4), 2543–2555 (2022)
- [20] Zeng, J., Tao, Y., Giese, T.J., York, D.M.: Qd $\pi$ : A quantum deep potential interaction model for drug discovery. *Journal of chemical theory and computation* **19**(4), 1261–1275 (2023)
- [21] Smith, J.S., Isayev, O., Roitberg, A.E.: Ani-1: an extensible neural network potential with dft accuracy at force field computational cost. *Chemical science* **8**(4), 3192–3203 (2017)
- [22] Rufa, D.A., Bruce Macdonald, H.E., Fass, J., Wieder, M., Grinaway, P.B., Roitberg, A.E., Isayev, O., Chodera, J.D.: Towards chemical accuracy for alchemical free energy calculations with hybrid physics-based machine learning/molecular mechanics potentials. *BioRxiv*, 2020–07 (2020)
- [23] Bartók, A.P., Kermode, J., Bernstein, N., Csányi, G.: Machine learning a general-purpose interatomic potential for silicon. *Physical Review X* **8**(4), 041048 (2018)
- [24] Deringer, V.L., Caro, M.A., Csányi, G.: A general-purpose machine-learning force field for bulk and nanostructured phosphorus. *Nature communications* **11**(1), 5461 (2020)
- [25] Wen, T., Zhang, L., Wang, H., Srolovitz, D.J., *et al.*: Deep potentials for materials science. *Materials Futures* **1**(2), 022601 (2022)
- [26] Jia, W., Wang, H., Chen, M., Lu, D., Lin, L., Car, R., Weinan, E., Zhang, L.: Pushing the limit of molecular dynamics with ab initio accuracy to 100 million atoms with machine learning. In: *SC20: International Conference for High Performance Computing, Networking, Storage and Analysis*, pp. 1–14 (2020). IEEE
- [27] Machaka, R.: Machine learning-based prediction of phases in high-entropy alloys. *Computational Materials Science* **188**, 110244 (2021)
- [28] Yang, M., Raucci, U., Parrinello, M.: Ammonia decomposition on lithium imide surfaces: a new paradigm in heterogeneous catalysis (2022)
- [29] Car, R., Parrinello, M.: Unified approach for molecular dynamics and density-functional theory. *Physical review letters* **55**(22), 2471 (1985)
- [30] Chanussot, L., Das, A., Goyal, S., Lavril, T., Shuaibi, M., Riviere, M., Tran, K., Heras-Domingo, J., Ho, C., Hu, W., *et al.*: Open catalyst 2020 (oc20) dataset and community challenges. *ACS Catalysis* **11**(10), 6059–6072 (2021)

- [31] Batatia, I., Kovacs, D.P., Simm, G., Ortner, C., Csányi, G.: Mace: Higher order equivariant message passing neural networks for fast and accurate force fields. *Advances in neural information processing systems* **35**, 11423–11436 (2022)
- [32] Park, Y., Kim, J., Hwang, S., Han, S.: Scalable parallel algorithm for graph neural network interatomic potentials in molecular dynamics simulations. *Journal of chemical theory and computation* **20**(11), 4857–4868 (2024)
- [33] Zhang, D., Bi, H., Dai, F.-Z., Jiang, W., Liu, X., Zhang, L., Wang, H.: Pretraining of attention-based deep learning potential model for molecular simulation. *npj Computational Materials* **10**(1), 94 (2024)
- [34] Zhang, D., Liu, X., Zhang, X., Zhang, C., Cai, C., Bi, H., Du, Y., Qin, X., Peng, A., Huang, J., *et al.*: Dpa-2: a large atomic model as a multi-task learner. *npj Computational Materials* **10**(1), 293 (2024)
- [35] Fu, X., Wood, B.M., Barroso-Luque, L., Levine, D.S., Gao, M., Dzamba, M., Zitnick, C.L.: Learning smooth and expressive interatomic potentials for physical property prediction. *arXiv preprint arXiv:2502.12147* (2025)
- [36] Yin, B., Wang, J., Du, W., Wang, P., Ying, P., Jia, H., Zhang, Z., Du, Y., Gomes, C., Duan, C., *et al.*: Alphanet: scaling up local-frame-based neural network interatomic potentials. *npj Computational Materials* **11**(1), 332 (2025)
- [37] Wood, B.M., Dzamba, M., Fu, X., Gao, M., Shuaibi, M., Barroso-Luque, L., Abdelmaqsoud, K., Gharakhanyan, V., Kitchin, J.R., Levine, D.S., *et al.*: Uma: A family of universal models for atoms. *arXiv preprint arXiv:2506.23971* (2025)
- [38] Shoghi, N., Kolluru, A., Kitchin, J.R., Ulissi, Z.W., Zitnick, C.L., Wood, B.M.: From molecules to materials: Pre-training large generalizable models for atomic property prediction. *arXiv preprint arXiv:2310.16802* (2023)
- [39] Kaplan, J., McCandlish, S., Henighan, T., Brown, T.B., Chess, B., Child, R., Gray, S., Radford, A., Wu, J., Amodei, D.: Scaling laws for neural language models. *arXiv preprint arXiv:2001.08361* (2020)
- [40] Hoffmann, J., Borgeaud, S., Mensch, A., Buchatskaya, E., Cai, T., Rutherford, E., Casas, D.d.L., Hendricks, L.A., Welbl, J., Clark, A., *et al.*: Training compute-optimal large language models. *arXiv preprint arXiv:2203.15556* (2022)
- [41] Zhang, D., Peng, A., Cai, C., Li, W., Zhou, Y., Zeng, J., Guo, M., Zhang, C., Li, B., Jiang, H., *et al.*: Graph neural network model for the era of large atomistic models. *arXiv preprint arXiv:2506.01686* (2025)
- [42] Narayanan, D., Shoeybi, M., Casper, J., LeGresley, P., Patwary, M., Korthikanti, V., Vainbrand, D., Kashinkunti, P., Bernauer, J., Catanzaro, B., *et al.*: Efficient large-scale language model training on gpu clusters using megatron-lm. In: *Proceedings of the International Conference for High Performance Computing, Networking, Storage and Analysis*, pp. 1–15 (2021)
- [43] Shoeybi, M., Patwary, M., Puri, R., LeGresley, P., Casper, J., Catanzaro, B.: Megatron-lm: Training multi-billion parameter language models using model parallelism. *arXiv preprint arXiv:1909.08053* (2019)
- [44] Shazeer, N., Mirhoseini, A., Maziarz, K., Davis, A., Le, Q., Hinton, G., Dean, J.: Outrageously large neural networks: The sparsely-gated mixture-of-experts layer. *arXiv preprint arXiv:1701.06538* (2017)
- [45] Fedus, W., Zoph, B., Shazeer, N.: Switch transformers: Scaling to trillion parameter models with simple and efficient sparsity. *Journal of Machine Learning Research* **23**(120), 1–39 (2022)
- [46] Lepikhin, D., Lee, H., Xu, Y., Chen, D., Firat, O., Huang, Y., Krikun, M., Shazeer, N., Chen, Z.: Gshard: Scaling giant models

- with conditional computation and automatic sharding. arXiv preprint arXiv:2006.16668 (2020)
- [47] Zoph, B., Bello, I., Kumar, S., Du, N., Huang, Y., Dean, J., Shazeer, N., Fedus, W.: St-moe: Designing stable and transferable sparse expert models. arXiv preprint arXiv:2202.08906 (2022)
- [48] Du, N., Huang, Y., Dai, A.M., Tong, S., Lepikhin, D., Xu, Y., Krikun, M., Zhou, Y., Yu, A.W., Firat, O., *et al.*: Glam: Efficient scaling of language models with mixture-of-experts. In: International Conference on Machine Learning, pp. 5547–5569 (2022). PMLR
- [49] Cai, W., Jiang, J., Wang, F., Tang, J., Kim, S., Huang, J.: A survey on mixture of experts in large language models. IEEE Transactions on Knowledge and Data Engineering (2025)
- [50] Artetxe, M., Bhosale, S., Goyal, N., Mihaylov, T., Ott, M., Shleifer, S., Lin, X.V., Du, J., Iyer, S., Pasunuru, R., *et al.*: Efficient large scale language modeling with mixtures of experts. arXiv preprint arXiv:2112.10684 (2021)
- [51] Dai, D., Deng, C., Zhao, C., Xu, R., Gao, H., Chen, D., Li, J., Zeng, W., Yu, X., Wu, Y., *et al.*: Deepseekmoe: Towards ultimate expert specialization in mixture-of-experts language models. arXiv preprint arXiv:2401.06066 (2024)
- [52] Levine, D.S., Shuaibi, M., Spotte-Smith, E.W.C., Taylor, M.G., Hasyim, M.R., Michel, K., Batatia, I., Csányi, G., Dzamba, M., Eastman, P., *et al.*: The open molecules 2025 (omol25) dataset, evaluations, and models. arXiv preprint arXiv:2505.08762 (2025)
- [53] Barroso-Luque, L., Shuaibi, M., Fu, X., Wood, B.M., Dzamba, M., Gao, M., Rizvi, A., Zitnick, C.L., Ulissi, Z.W.: Open materials 2024 (omat24) inorganic materials dataset and models. arXiv preprint arXiv:2410.12771 (2024)
- [54] Clark, K., Khandelwal, U., Levy, O., Manning, C.D.: What does bert look at? an analysis of bert’s attention. arXiv preprint arXiv:1906.04341 (2019)

## Contents

<b>1</b>	<b>Hyperparameters and System Configurations</b>	<b>1</b>
<b>2</b>	<b>Energy and Force MAE value</b>	<b>1</b>

### Supplementary Note 1. Hyperparameters and System Configurations

The baseline 6-layer DPA3 model utilizes hyperparameters summarized in Table 1, following the standard configuration established in the DPA3 paper [1]. However, batch sizes were adjusted according to the dataset: a batch size of 256 was used for OMol25, while 128 was used for both OMat24 and OC20M.

**Supplementary Table 1** | Hyper parameters for 6-layer DPA3 model.

Hyper-parameters	baseline
Number of update layers $L$	6
Maximum graph order $k$	2
Dimension of vertex features in $G^{(0)}$	128
Dimension of vertex features in $G^{(1)}$	64
Dimension of vertex features in $G^{(2)}$	32
Cutoff radius in $G^{(1)}$ Å	6.0
Cutoff radius in $G^{(2)}$ Å	4.0
Batch size	128/256
Optimizer	AdamW
Learning rate scheduling	Exp
Maximum learning rate	1e-3
Minimum learning rate	1e-5
Number of training steps	1M
Activation Function Threshold	10.0
Loss function	MSE

The model dimensions are scaled to create larger baselines: for the “4× params baseline”, the dimensions of  $G^{(0)}$ ,  $G^{(1)}$ , and  $G^{(2)}$  are doubled from 128, 64, and 32 to 256, 128, and 64, respectively. Similarly, the “6× params baseline” is constructed by expanding these dimensions to 314, 156, and 78.

The hyperparameters for the MoE and MoLE models are identical to the baseline model. Further implementation details specific to the MoE and MoLE architectures are provided in the main text.

### Supplementary Note 2. Energy and Force MAE value

While the majority of results in the main text are reported as normalized MAEs, this section provides the absolute MAE values for direct comparison. Specifically, Table 2 details the energy and force MAEs for the MoE-E model across different numbers of activated experts  $K$ , corresponding to the trends visualized in Fig. 2(a).

Similarly, Table 3 summarizes the performance metrics for both MoLE-E and MoE-E. This table provides the numerical data supporting the trends visualized in Fig. 2(b) of the main text. Table 4 compares Global and Element-wise routing, offering the specific values corresponding to the summary in Table 1. Finally, Table 5 presents the energy and force MAEs for different datasets, corresponding to the results visualized in Fig.3.

**Supplementary Table 2** | Performance comparison of different configurations with varying numbers of shared experts.

MoE-E	Shared Experts	Energy MAE (eV)	Force MAE (eV Å <sup>-1</sup> )
Baseline	–	8.43e-3	5.89e-2
$K = 2$	0	9.12e-3	5.68e-2
	1	7.92e-3	5.37e-2
$K = 4$	0	8.14e-3	5.41e-2
	2	6.50e-3	4.59e-2
	3	6.47e-3	4.65e-2
$K = 6$	0	7.78e-3	5.31e-2
	2	5.99e-3	4.51e-2
	3	6.24e-3	4.40e-2
	4	6.16e-3	4.41e-2
$K = 8$	0	7.81e-3	5.30e-2
	2	6.15e-3	4.47e-2
	4	5.68e-3	4.21e-2
	6	5.54e-3	4.13e-2

**Supplementary Table 3** | Performance comparison of different configurations with varying numbers of shared experts.

Structure	Share Experts	Experts	Energy MAE (eV)	Force MAE (eV Å <sup>-1</sup> )
Baseline	–	–	8.43e-3	5.89e-2
4× params Baseline	–	–	6.90e-3	4.89e-2
MoLE-E	0	4	8.65e-3	5.74e-2
		16	8.10e-3	5.52e-2
		64	8.29e-3	5.50e-2
	2	4	7.70e-3	5.38e-2
		16	7.14e-3	5.04e-2
		64	7.30e-3	4.99e-2
$K = 4$ MoE-E	0	4	8.80e-3	5.59e-2
		16	8.12e-3	5.43e-2
		64	8.14e-3	5.41e-2
	2	4	6.86e-3	4.76e-2
		16	6.58e-3	4.67e-2
		64	6.50e-3	4.59e-2

**Supplementary Table 4** | Energy and Force MAE values. The results compare the performance of Global (G) vs. Element-wise (E) routing across different expert counts.

Model	Routing	Energy MAE(eV)			Force MAE (eV Å <sup>-1</sup> )		
		4 Experts	16 Experts	64 Experts	4 Experts	16 Experts	64 Experts
MoLE	Global (G)	8.27e-3	7.98e-3	8.03e-3	5.68e-2	5.51e-2	5.59e-2
	Element-wise (E)	7.70e-3	7.14e-3	7.30e-3	5.38e-2	5.04e-2	4.99e-2
MoE	Global (G)	N/A	N/A	N/A	N/A	N/A	N/A
	Element-wise (E)	6.86e-3	6.58e-3	6.50e-3	4.76e-2	4.67e-2	4.59e-2

**Supplementary Table 5** | Performance comparison: Model across different datasets

Model	OMol25		OMat24		OC20M	
	Energy MAE	Force MAE	Energy MAE	Force MAE	Energy MAE	Force MAE
Baseline	0.0084	0.0589	0.0219	0.1078	0.0066	0.0775
6× Params	0.0065	0.0461	0.0200	0.1006	0.0053	0.0667
MoLE-E	0.0071	0.0501	0.0195	0.1019	0.0050	0.0661
MoE-E	0.0062	0.0440	0.0191	0.0983	0.0048	0.0630

\* Energy MAE in eV, Force MAE in eV/Å.

### Supplementary References

- [1] Duo Zhang, Anyang Peng, Chun Cai, Wentao Li, Yuanchang Zhou, Jinzhe Zeng, Mingyu Guo, Chengqian Zhang, Bowen Li, Hong Jiang, et al. Graph neural network model for the era of large atomistic models. *arXiv preprint arXiv:2506.01686*, 2025.